IOP Conf. Series: Journal of Physics: Conf. Series **837** (2017) 012009 doi:10.1088/1742-6596/837/1/012009

Theoretical Models of Protostellar Binary and Multiple Systems with AMR Simulations

Tomoaki Matsumoto[1], Kazuki Tokuda[2], Toshikazu Onishi[2], Shu-ichiro Inutsuka[3], Kazuya, Saigo[2], Shigehisa Takakuwa[4],

[1] Faculty of Sustainability Studies, Hosei University, Fujimi, Chiyoda-ku, Tokyo 102-8160, Japan
[2] Department of Physical Science, Graduate School of Science, Osaka Prefecture University, 1-1 Gakuen-cho, Naka-ku, Sakai, Osaka 599-8531, Japan
[3] Department of Physics, Nagoya University, Chikusa-ku, Nagoya 464-8602, Japan
[4] Department of Physics and Astronomy, Graduate School of Science and Engineering, Kagoshima University, 1-21-35 Korimoto, Kagoshima 890-0065, Japan

E-mail: matsu@hosei.ac.jp

Abstract. We present theoretical models for protostellar binary and multiple systems based on the high-resolution numerical simulation with an adaptive mesh refinement (AMR) code, SFUMATO. The recent ALMA observations have revealed early phases of the binary and multiple star formation with high spatial resolutions. These observations should be compared with theoretical models with high spatial resolutions. We present two theoretical models for (1) a high density molecular cloud core, MC27/L1521F, and (2) a protobinary system, L1551 NE. For the model for MC27, we performed numerical simulations for gravitational collapse of a turbulent cloud core. The cloud core exhibits fragmentation during the collapse, and dynamical interaction between the fragments produces an arc-like structure, which is one of the prominent structures observed by ALMA. For the model for L1551 NE, we performed numerical simulations of gas accretion onto protobinary. The simulations exhibit asymmetry of a circumbinary disk. Such asymmetry has been also observed by ALMA in the circumbinary disk of L1551 NE.

1. Introduction

Most of low-mass young stars are members of multiple systems of two or more stars, and multiple star formation is considered to be a major mode of low-mass star formation [1]. Recent high-resolution observations with Atacama Large Millimeter/Submillimeter Array (ALMA) have revealed early phase of low-mass star formation. In order to compare these detailed observations with numerical simulations, the numerical simulations should be performed also with a high-resolution. An adaptive mesh refinement (AMR) technique allows us to obtain a local high resolution for grid-based numerical simulations [2]. In this paper, we report two cases of numerical models for comparison with the recent ALMA observations.

The first case is for a dense core in the Taurus molecular cloud, MC27 or L1521F [3, 4]. Observations have suggested that MC27/L1521F is in a very early stage of star formation [5]. The recent ALMA Cycle 0 and 1 observations toward MC27/L1521F has been carried out [6, 7], and revealed an arc structure with a length of $\sim$ 2000 au at the center of the cloud core [6]. In order to investigate the origin of the arc structure, we performed numerical simulations for protostellar collapse of cloud cores [8].

The second case is for a protobinary system, L1551 NE, which is a class I object located in the Taurus region. The recent ALMA Cycle 0 observations have resolved fine structures around the protobinary stars: a circumstellar disk around each star and a circumbinary disk around the binary stars [9]. We performed numerical simulations for gas accretion onto binary stars in order to investigate complex structures around the binary stars.

2. A high-density molecular cloud core, MC27/L1521F

2.1. Models and methods

As the initial condition, a filamentary molecular cloud is considered because recent observations have shown that molecular clouds often exhibit filamentary structures [10, 11, 12]. The filament is assumed to be infinitely long and in an equilibrium state where thermal pressure supports an isothermal cloud against its self-gravity. The filamentary cloud has a density distribution of $\rho(R) = \rho_0(1+R^2/R_0^2)^{-2}$ [14, 13] with $R_c = 0.05\,\mathrm{pc}$ and $\rho_0 = 2c_s^2/(\pi G R_0^2) = 1.45\times10^{-19}\,\mathrm{g\,cm^{-3}}$ (the corresponding number density is $n_0 = 3.79\times10^4\,\mathrm{cm^{-3}}$), where the isothermal sound speed is assumed as $c_s = 0.190\,\mathrm{km\,s^{-1}}$ and the corresponding gas temperature is $T = 10\,\mathrm{K}$. The radius of the cloud R_c comes form a typical width of filamentary clouds indicated by the Herschel survey [11]. For comparison, we performed other simulations assuming a spherical cloud, and confirmed that the main results described in this section are insensitive to the initial cloud shape.

Turbulence was imposed at the initial stage, of which velocity field is incompressible with a power spectrum of $P(k) \propto k^{-4}$, generated according to [15], where k is the wavenumber. This power spectrum results in a velocity dispersion of $\sigma(\lambda) \propto \lambda^{1/2}$, in agreement with the Larson scaling relations [16]. The barotropic equation of state was assumed to be $P(\rho) = c_s^2\rho + \kappa\rho^{7/5}$ with $\kappa = c_s^2\rho_{\rm cr}^{-2/5}$, where the critical density is set at $\rho_{\rm cr} = 10^{-13}\,\mathrm{g\,cm^{-3}}$ (the corresponding number density is $n_{\rm cr} = 2.62\times10^{10}\,\mathrm{cm^{-3}}$), which was taken from the numerical results of [17]. The gas is approximated to be isothermal for $\rho \lesssim \rho_{\rm cr}$ and the gas temperature increases adiabatically with the density for $\rho \gtrsim \rho_{\rm cr}$. The adopted equation of state does not take into account shock heating, because we implicitly assume that the shocked gas is instantaneously cooled by emission of radiation. The magnetic field was ignored for simplicity.

A three-dimensional AMR code, SFUMATO [18], was employed as a simulation code. The hydrodynamic scheme was modified to have a third order of accuracy in space and a second order in time. The MUSCL scheme with the MINMOD limiter is adopted, and it has a first order accuracy only at the discontinuities. The self-gravity of the gas is solved by the multigrid method. The computational domain is resolved on a base grid of $l = 0$ with 256^3 cells. The maximum grid level was set at $l = 11$. The cell width is $\Delta x_{\rm min} = 0.613$ au on the finest grid of $l = 11$, and $\Delta x_{\rm max} = 1.26\times10^3$ au on the base grid of $l = 0$. The Jeans condition was employed as a refinement criterion [19]; blocks are refined when the Jeans length is shorter than 8 times the cell width, i.e., $\lambda_J < 8\Delta x$, where λ_J is the Jeans length.

The sink particles were employed as a sub-grid model of protostars. The detailed implementations of the sink particles are shown in [20]. The critical density for the sink particle formation is set at $\rho_{\rm sink} = 1\times10^{-11}\,\mathrm{g\,cm^{-3}}$ ($n_{\rm sink} = 2.62\times10^{12}\,\mathrm{cm^{-3}}$), and the sink radius is set at $r_{\rm sink} = 4\Delta x_{\rm min} = 2.45$ au.

2.2. Results

Figure 1 shows the column density distribution on four different spatial scales at the stage of $t_p = 1.760\times10^4$ yr, where t_p denotes the time after the first sink particle formation. The simulation shows that the initial filamentary cloud fragments into several cloud cores as shown in Figure 1a. A cloud core undergoes gravitational collapse to exhibit a sharply peaked density distribution (Figure 1b) in agreement with molecular line observations toward MC27/L1521F [5]. In the early phase, the cloud core fragments into four gas condensations, which evolve into four protostars (sink particles). Two sink partices merge because of their chaotic orbits,

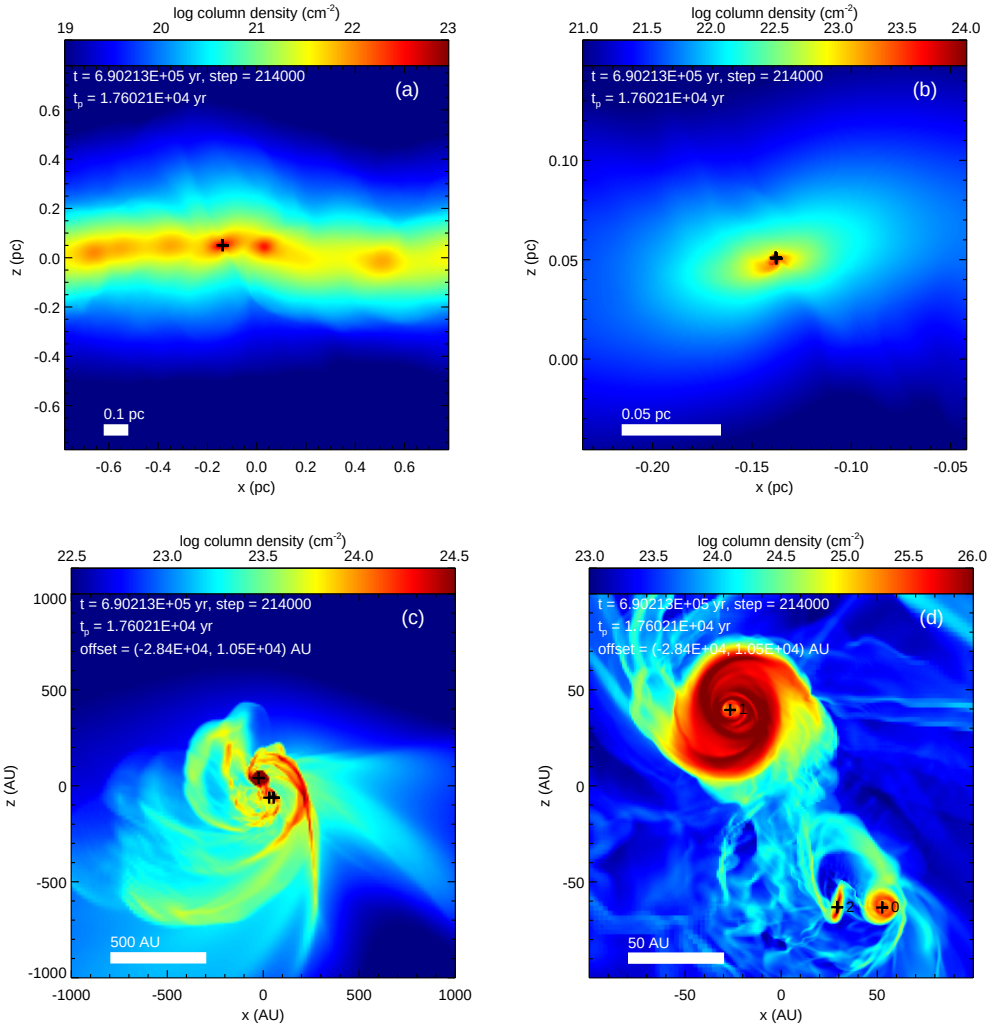

Figure 1. Column density distribution along the y-direction on four different spatial scales at $t = 0.690$ Myr ($t_p = 1.760 \times 10^4$ yr). The color scales depict the column densities. The black crosses indicate the positions of the sink particles. In panels (c) and (d), the coordinates are offset so that the center of each panel coincides with the center of mass of the sink particles. The sink particles are labeled with identification numbers 0, 1, and 2 in panel (d). Taken from [8].

and three sink particles survive to form a triple system as shown in Figures 1c and 1d. Every protostar has a circumstellar disk around it. The most massive protostar, which is labeled 1, has the largest disk. The other protostars have small disks because successive close encounters between protostars 0 and 2 prevent growth of the circumstellar disks around them.

The simulation reproduces formation of a triple system. The ALMA observations have also revealed a similar system: a protostar and two gas condensation at the center of the MC27/L1521F [6].

The simulation exhibits arc structures in the infalling envelope as shown in Figure 1c. The arc structures extend up to a 1000 au scale in agreement with the ALMA observations [6]. These structures are caused by the gravitational interaction between the sink particles and the envelope gas. The gas is accelerated by the gravitational torque from the orbiting protostars.

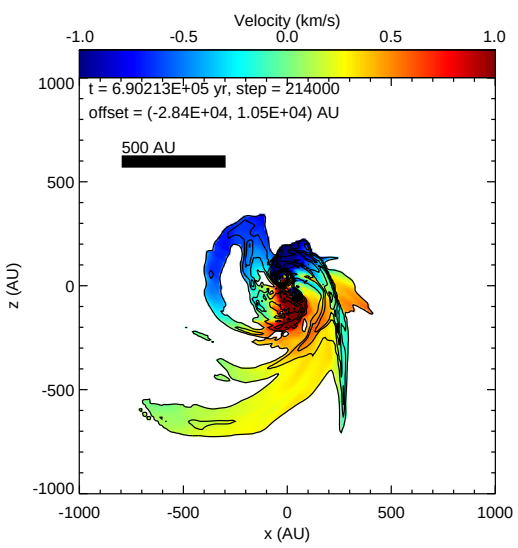

Figure 2. Line-of-sight velocity distribution in the arc structures. The color scale shows the density-weighted velocity along the line of sight. The contour shows the column density on a logarithmic scale with $\log(N/\mathrm{cm}^{-2}) = 23.4, 23.6, \cdots$, where N denotes the column density. The velocity is shown only in the regions where the column density is greater than the lowest contour level. Taken from [8].

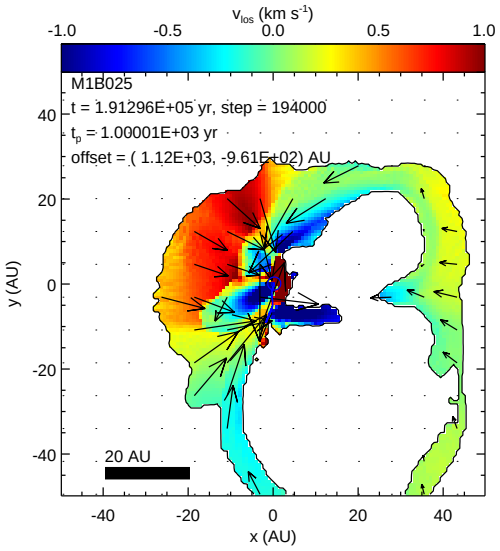

Figure 3. Line-of-sight velocity distribution of the magnetic walls in MHD simulations. The color scale shows the density-weighted velocity distribution along the line of sight (the z-direction). The arrows denote the density-weighted velocity on the $x-y$ plane. The black contour is an outline of a volume of $\rho \geq \rho_{\mathrm{cr}}$.

Figure 2 shows line-of-sight velocity distribution in the arc structures. This figure is comparable to Figure 4 of [6]. The velocity ranges typically from $-0.5\,\mathrm{km\,s^{-1}}$ to $0.5\,\mathrm{km\,s^{-1}}$ in agreement with the observation. This suggests that the observed arc structure in MC27/L1521F is caused by the gravitational interaction as shown in the simulation.

We performed another simulation, taking account of magnetic field [22]. The initial magnetic field is assumed to be uniform, and a relatively strong magnetic field is assumed with a mass-to-flux ratio of 1.12. The MHD simulations also reproduce arc structures as shown in Figure 3. The arc structures are caused by magnetic walls, which have been predicted by the theoretical arguments [23] and the one-dimensional MHD simulations [24]. The MHD simulations however do not reproduce multiple dense gas condensations, which are observed at the center of MC27/L1521F [6]. This is because the magnetic field suppresses fragmentation of cloud cores in typical cases in agreement with the previous MHD simulations [21]. If the observed dense gas condensations are produced by fragmentation of the cloud core, the magnetic field is weak enough to promote fragmentation of the cloud core.

3. A binary protostar system, L1551 NE

3.1. Models and methods

L1551 NE is a protobinary system embedded in the envelope gas, and the outflows are associated with the protobinary stars, suggesting that the protobinary stars actively accrete the gas of the envelope. In order to mimic this protobinary system, we consider the situation where the gas is

injected at the computational boundaries, and it falls onto the protobinary stars.

In the three-dimensional computational domain of $[-12D, 12D]^2 \times [-6D, 6D]$, two protostars are considered, of which barycenter is located at the origin, where $D = 145$ au is a binary separation of L1551 NE. The coordinates of the primary and secondary stars are therefore $(x, y, z) = (-M_2 D/M_{\rm tot}, 0, 0)$ and $(x, y, z) = (M_1 D/M_{\rm tot}, 0, 0)$, respectively, where M_1 and M_2 are masses of the primary and secondary stars, and $M_{\rm tot} = M_1 + M_2$ is a total mass of the binary stars. The total mass and mass ratio are set at $M_{\rm tot} = 0.8 M_\odot$ and $M_2/M_1 = 0.19$ according to the observations [25].

Gas with a constant density and a specific angular momentum is injected at the cylindrical boundaries: the cylindrical surface of $R = 12D$, and the top and bottom surfaces of $z = \pm 6D$. On these surfaces, the gas has a radial velocity of $v_r = [2GM_{\rm tot}/r - (j_{\rm inf}/R)^2]^{1/2}$, assuming a freefall from an infinity direction, where $j_{\rm inf}$ is the specific angular momentum of the gas, r is the spherical radius, and R is the cylindrical radius. When the centrifugal force is larger than the gravity ($j_{\rm inf}^2/R^3 > GM_{\rm tot}R/r^3$), no gas is injected there, corresponding the centrifugal barrier. These boundary conditions are similar to those of [26]. The specific angular momentum of the injected gas is given by $j_{\rm inf} = (GM_{\rm tot}R_{\rm cent})^{1/2}$, where $R_{\rm cent}(= 300$ au) is the centrifugal radius as determined from the observations [25, 27]. For simplicity, an isothermal gas is assumed with a sound speed of $c_s = 0.1(GM_{\rm tot}/D)^{1/2} = 0.221\,{\rm km\,s^{-1}}$. The gas temperature is therefore 13.5 K, which is typical for dense molecular cloud cores and infalling envelopes.

A three-dimensional AMR code, SFUMATO [18], was employed. The hierarchical grid was fixed during the calculation, and a so-called fixed mesh refinement (FMR) was adopted. The grid configuration is shown in Figure 4. The block size is set at 16^3 cells, and the computational domain is resolved by $8^2 \times 4$ blocks. The base grid of $l = 0$ therefore has a size of $128^2 \times 64$. The cell width is $\Delta x_{\rm min} = 0.85$ au on the finest grid of $l = 5$, and $\Delta x_{\rm max} = 27$ au on the base grid of $l = 0$.

The binary protostars are represented by two sink particles. The sink particles accrete gas within a given radius of $4\Delta x_{\rm min} = 3.4\,{\rm au}$. The simulation was performed on a rotating frame where the sink particles are at rest, taking into account both the centrifugal and Coriolis forces. The calculation was halted at ~ 250 rotations of the binary orbit.

3.2. Results

The simulation shows that the injected gas falls toward the center, and the angular momentum prevents the gas from falling into the binary stars directly, providing a circumbinary disk with a central gap. The gravitational torque from the orbiting binary stars produces the spiral arms in the circumbinary disk, and it also induces accretion onto the circumstellar disks (Figure 5). The gases in each circumstellar disk rotates in circular orbits around the sink particle. The angular momenta are transported presumably because of numerical viscosity and the gas finally falls onto the sink particle. Similar structures have been also shown in the many previous simulations [28, 26, 29, 30, 31].

Based on the simulation here, observational visualization was performed to compare the simulation with the observation [9]. The comparison indicates that the observed velocity features exhibits qualitative agreement with those associated with the spiral arms in the numerical simulations. L1551 NE has active outflows, implying that the magnetic fields play an important role in the acceleration of the outflow in the regions near the protostars. The hydrodynamical model presented here should be extended to MHD models in order to investigate the effects of the magnetic fields on the circumbinary structure.

The ALMA observations toward L1551 NE suggest that the circumbinary disk on the secondary side is brighter than on the primary side [9]. Such an asymmetry of a circumbinary disk has been also observed toward a class II binary, UY Aur [32]. Asymmetry in the circumbinary disk is reproduced in the numerical simulation here. Figure 5 shows asymmetry

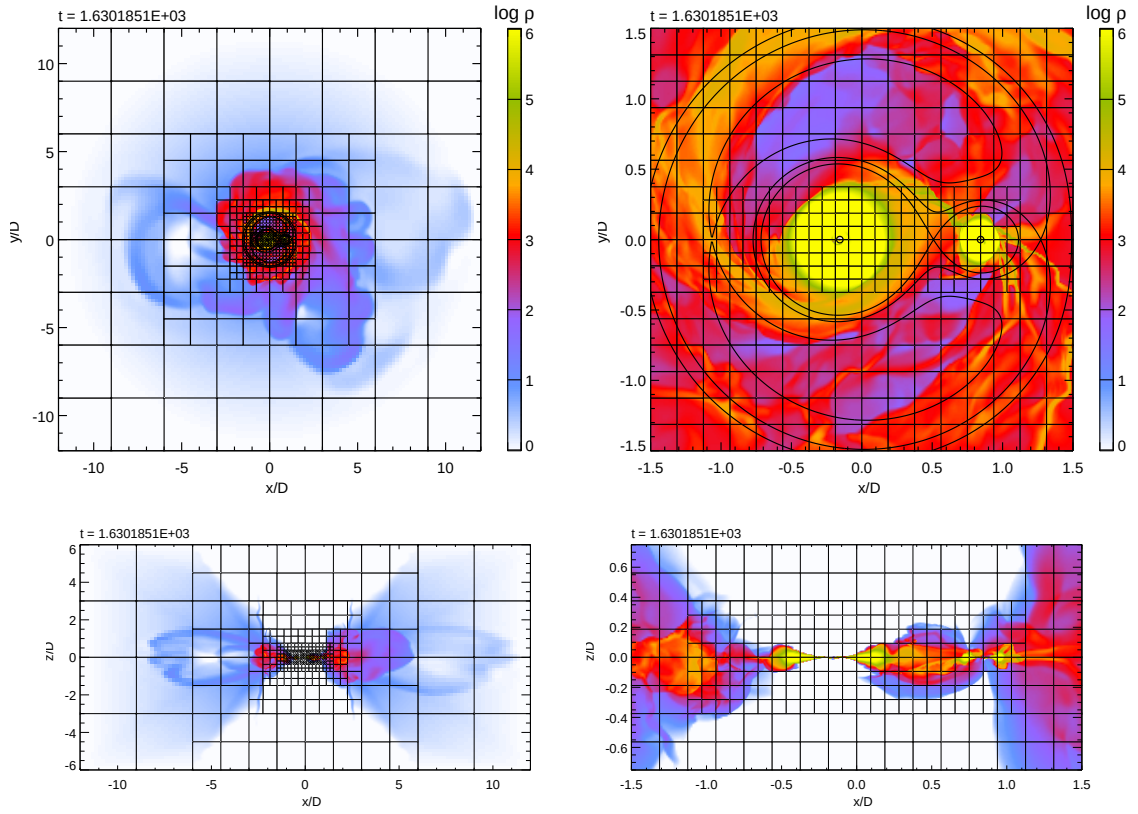

Figure 4. A snapshot of the simulation for binary accretion. The upper panels show the density distributions in logarithmic scale in the $z = 0$ plane, while the lower panels show those in the $y = 0$ plane. The right panels are enlargements of the left panels. The The black horizontal and vertical lines are the boundaries of the AMR blocks. In upper panels, the contours of the Roche potential are shown for comparison.

in the circumbinary disk, where the surface density is higher on the secondary side (the right side) than on the primary side (the left side) in this snapshot. The asymmetric structure rotates with respect to the position angle of the binary stars. Figure 6 shows the surface density as a function of time in a ring region with a radius of $R = (2 \pm 0.1)D$, indicating that the asymmetric structure rotates with an angular velocity of $\Omega = \Omega_\star/4$, where $\Omega_\star$ is an angular velocity of the binary orbit. Such commensurability between the asymmetric circumbinary disk and the binary orbit indicates a resonance caused by the gravitational torque from the binary stars

4. Summary

We performed numerical simulations for modeling of the recent ALMA observations toward a high-density molecular cloud core, MC27/L1521F, and a binary protostar system, L1551 NE. The AMR technique was adopted for the numerical simulations to obtain a high resolution because the corresponding ALMA observations also exhibit a high spatial resolution. The numerical simulations for MC27/L1521F suggest that the observed dense gas condensations are caused by fragmentation of the cloud core, and the arc structure is a consequence of the dynamical interaction between the fragments and the infalling envelope. The numerical simulations for L1551 NE suggest that existence of the spiral arms in the circumbinary disk. The simulations also exhibit asymmetry in the circumbinary disk, which is caused by the resonance

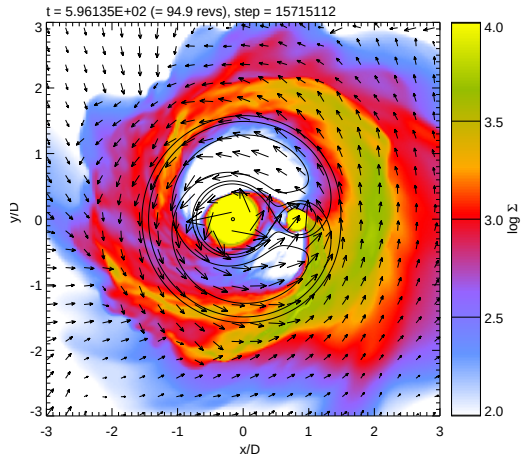

Figure 5. Surface density of the central box of $[-3D, 3D]^2 \times [-1.5D, 1.5D]$. The arrows denote the velocity distribution in the $z = 0$ plane. The velocity in the rest frame is plotted.

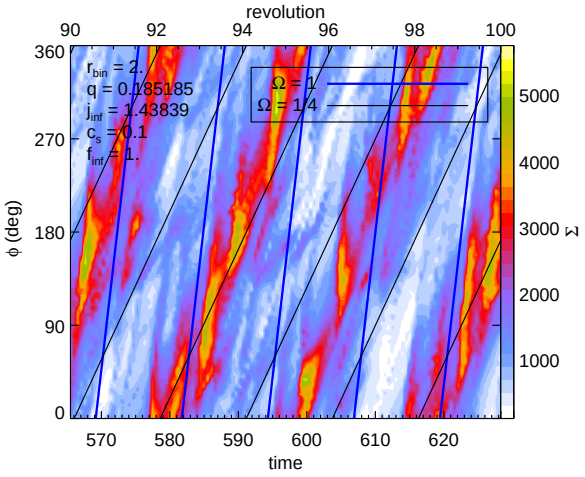

Figure 6. Surface density distribution within a thin ring with a radius of $R = (2 \pm 0.1)D$. The ordinate and abscissa denote the azimuthal angle ϕ and time t, respectively. The stages between 90 and 100 binary periods are shown. Blue and black lines show the relationships of $\phi = \Omega t$ with $\Omega = \Omega_\star$ and $\Omega_\star/4$, respectively.

of the rotation of the circumbinary disk and the binary orbit.

Acknowledgments

Numerical computations were carried out on Cray XC30 at the Center for Computational Astrophysics, National Astronomical Observatory of Japan. This research was supported by JSPS KAKENHI Grant Numbers 26400233, 26287030, 24244017, 23540270.

References

[1] Reipurth, B., Clarke, C. J., Boss, A. P., et al. 2014, Protostars and Planets VI, 267
[2] Berger, M. J., & Colella, P. 1989, Journal of Computational Physics, 82, 64
[3] Mizuno, A., Onishi, T., Hayashi, M., et al. 1994, Nature, 368, 719
[4] Codella, C., Welser, R., Henkel, C., Benson, P. J., & Myers, P. C. 1997, A&A, 324, 203
[5] Onishi, T., Mizuno, A., & Fukui, Y. 1999, PASJ, 51, 257
[6] Tokuda, K., Onishi, T., Saigo, K., et al. 2014, ApJL, 789, L4
[7] Tokuda, K., Onishi, T., Matsumoto, T., et al. 2016, ApJ, 826, 26
[8] Matsumoto, T., Onishi, T., Tokuda, K., & Inutsuka, S.-i. 2015, MNRAS, 449, L123
[9] Takakuwa, S., Saito, M., Saigo, K., et al. 2014, ApJ, 796, 1
[10] André, P., Men'shchikov, A., Bontemps, S., et al. 2010, A&A, 518, L102
[11] Arzoumanian, D., André, P., Didelon, P., et al. 2011, A&A, 529, L6
[12] Hacar, A., Tafalla, M., Kauffmann, J., & Kovács, A. 2013, A&A, 554, A55
[13] Ostriker, J. 1964, ApJ, 140, 1056
[14] Stodólkiewicz, J. S. 1963, Acta Astron., 13, 30
[15] Dubinski, J., Narayan, R., & Phillips, T. G. 1995, ApJ, 448, 226
[16] Larson, R. B. 1981, MNRAS, 194, 809
[17] Masunaga, H., Miyama, S. M., & Inutsuka, S. 1998, ApJ, 495, 346.
[18] Matsumoto, T. 2007, PASJ, 59, 905
[19] Truelove, J. K., Klein, R. I., McKee, C. F., Holliman, J. H., II, Howell, L. H., & Greenough, J. A. 1997, ApJL, 489, L179

[20] Matsumoto, T., Dobashi, K., & Shimoikura, T. 2015, ApJ, 801, 77
[21] Machida, M. N., Matsumoto, T., Hanawa, T., & Tomisaka, K. 2005, MNRAS, 362, 382
[22] Matsumoto, T., Machida, M. N., & Inutsuka, S.-i. 2016 in preparation
[23] Li, Z.-Y., & McKee, C. F. 1996, ApJ, 464, 373
[24] Tassis, K., & Mouschovias, T. C. 2005, ApJ, 618, 783
[25] Takakuwa, S., Saito, M., Lim, J., et al. 2012, ApJ, 754, 52
[26] Bate, M. R., & Bonnell, I. A. 1997, MNRAS, 285, 33
[27] Takakuwa, S., Saito, M., Lim, J., & Saigo, K. 2013, ApJ, 776, 51
[28] Artymowicz, P., & Lubow, S. H. 1996, ApJL, 467, L77
[29] Ochi, Y., Sugimoto, K., & Hanawa, T. 2005, ApJ, 623, 922
[30] Gómez de Castro, A. I., López-Santiago, J., Talavera, A., Sytov, A. Y., & Bisikalo, D. 2013, ApJ, 766, 62
[31] Young, M. D., Baird, J. T., & Clarke, C. J. 2015, MNRAS, 447, 2907
[32] Tang, Y.-W., Dutrey, A., Guilloteau, S., et al. 2014, ApJ, 793, 10